Available online at www.sciencedirect.com

jmr&t Journal of Materials Research and Technology

journal homepage: www.elsevier.com/locate/jmrt

Original Article

Effect of nanostructure on phase transformations during heat treatment of 2024 aluminum alloy

K. B. Demétrio [a,*], A.P. G. Nogueira [b], C. Menapace [b], T. Bendo [c], A. Molinari [b]

[a] Postgraduate Program in Materials Science and Engineering, University of the South of Santa Catarina, Av. Universitaria, 1105, 88806-000, Criciuma, SC, Brazil

[b] Department of Material Engineering and Industrial Technologies, University of Trento, Via Mesiano 77, 38100, Italy

[c] UFSC, LabMat — Materials Laboratory, Bloco B-Eng. Mecânica, Florianópolis, SC, 88040900, Brazil

ARTICLE INFO

Article history:
Received 18 December 2020
Accepted 9 July 2021
Available online 21 July 2021

Keywords:
Cryomilling
2024 Al alloy
Nanostructured
Thermal stability
Artificial aging
Phase transformation

ABSTRACT

In this work, we studied the transformations involving the coherent (θ"/S"), semicoherent (θ'/S'), and incoherent (θ/S) precipitates (θ = Al_2Cu, S = Al_2CuMg) formed during the heat treatment of an annealed nanostructured powder of Al 2024 produced by cryogenic milling. These precipitates form over a wide temperature range (300–500 °C) depending on the chemical composition. They influence grain growth during sintering and may facilitate the formation of a fully dense nanostructured material. Mechanical milling was performed for 20 h at a cryogenic temperature to obtain nanostructured particles. The structural evolution and morphology of the particles during the heat treatment were investigated for three particle size ranges (<25, 25–45, and 45–90 μm). Heat treatment of the milled powder was performed at three different temperatures (475, 500, and 525 °C) for 5, 10, 15, and 20 min. Morphological analysis of the as-milled particles using scanning electron microscopy indicated that the milling process was not completed. X-ray diffraction analysis yielded the θ and S volume fractions for the heat-treated and as-milled powders. DSC analysis indicated the precipitation and dissolution of GP (Guinier-Preston zone), coherent, and incoherent precipitates during heating of the as-atomized and milled powders.

Accumulation of the deformation energy during milling is suggested to lead to an early transformation of the S and θ phases in the finer powder.

1. Introduction

The mechanical properties and superplasticity of Al alloys can be improved by refining their microstructure to the nanometer scale [1–3]. Many techniques have been developed in the field of powder metallurgy for producing nanomaterials. For instance, it is possible to produce a nanostructured Al alloy by milling (ball or cryomilling) a prealloyed powder. Further, hot isostatic pressing, dynamic consolidation, hot extrusion, and

* Corresponding author.
E-mail address: ketnerbd@gmail.com (K. B. Demétrio).
https://doi.org/10.1016/j.jmrt.2021.07.044

spark plasma sintering (SPS) are techniques that can be used to finally obtain a fully dense material with minimal grain growth [4–12]. SPS has been used by some researchers to sinter nanostructured ferrous and aluminum powders [13–16].

Several Al alloys are hardened by the precipitation of coherent, semicoherent, and incoherent precipitates, which are formed during heat treatment. Based on the chemical composition of the alloy, these precipitates can form between 100 and 500 °C and prevent grain growth during the sintering process [14].

According to Badini et al. [15], two different precipitation sequences can occur either separately or simultaneously in the 2024 Al alloy, depending on the Cu/Mg ratio in the alloy. During the artificial aging of this alloy, Al–Cu and/or Al–Cu–Mg phases are formed. At high temperatures and/or after prolonged heat treatments, stable incoherent phases of Al_2Cu (θ) and/or Al_2CuMg (S) are formed. The decomposition of the supersaturated Al–Cu solid solution, which has a face centered cubic crystalline structure, results in the formation of the following phases: Guinier–Preston (GP) zone → θ" → θ' → θ (Al_2Cu) [15–17]. Similarly, in the case of the Al–Cu–Mg system, the decomposition of the supersaturated Al–Cu–Mg solid solution occurs in the following precipitation sequence: Guinier–Preston–Bagaryatsky (GPB) zone → S' → S (Al_2CuMg with orthorhombic crystalline structure) [15,17–20].

To achieve near-full density, the nanostructured Al alloy powder is sintered by SPS at 500–550 °C [4], depending on the pressure available in the SPS apparatus. In the present work, heat treatments were carried out in the above-mentioned temperature range to investigate the microstructural transformations occurring during the corresponding SPS cycles. The heat-treatment temperatures were well above the stability range of the GP zones and coherent precipitates; therefore, the characterization of the treated specimens was carried out by X-ray diffraction (XRD) analysis, which can detect the incoherent phases. The precipitates in the powder can withstand grain growth during sintering, favoring the preservation of the original nanostructure. Therefore, the focus of this work was on the transformation of the precipitates, particularly, on the effect of the nanostructure and the lattice strain on the transformations. Hence, the experiments were carried out on milled powders with different crystallite sizes and residual strains.

2. Experimental procedures

A 2024 Al alloy powder (4.0 wt% Cu, 1.5 wt% Mg, 0.5 wt% Si, 0.6 wt% Mn, 0.1 wt% Fe, balance Al) produced from granules (Ecka Granules Metal Powders Ltd.) via spray atomization was used in this work. Following the procedure described by Lee et al. [21], nanostructured powder particles were formed via low-energy mechanical milling performed at a cryogenic temperature (−193 °C) using stainless steel balls (6.4 mm in diameter) in a stainless steel vial by maintaining a ball-to-powder ratio of 4:1. Basing on the approach developed by Molinari et al. [4], cryomilling was performed in a modified Union Process attritor 01-HD mill at 300 rpm for 20 h. Samples were taken after 3, 6, 9, and 20 h. During the milling process, liquid nitrogen was added to the stainless-steel container such that the powder and balls were fully immersed in it. The liquid nitrogen was also used as a lubricant, and no other process control agent was employed [5,22,23].

After being milled for 20 h, the powder was transferred to a glove box in an argon atmosphere for evaporating the nitrogen [23]. Next, the as-atomized and milled powders were sieved in five different particle size ranges. Only the powder samples corresponding to the three smaller size ranges (<25 μm, 25–45 μm, and 45–90 μm) were used for the study. The particle size distribution was determined by weighing the powders after prolonged sieving using an analytical balance with a sensitivity of 0.1 μg. The powder morphologies were characterized using a scanning electron microscopy (SEM) instrument (Supra 40 ZEISS, GEMINI column®). Next, the samples were subjected to differential scanning calorimetry (DSC) in an argon atmosphere, which was performed in an oven at a heating rate of 20 °C/min to simulate the precipitation-inducing thermal treatment. The DSC curves for Al alloys reported by Badini et al. [15], Murayama et al. [19], Jana et al. [20], Papazian [24], and Khitouni et al. [25] were used as references to interpret the DSC data. Finally, heat treatments were performed on the powders to study the formation of precipitates under different conditions. The treatments were conducted under a high vacuum ($1{,}3333*10^{-5}$ mbar) at three different temperatures (475, 500, and 525 °C) and for four different periods (5, 10, 15, and 20 min).

XRD analysis was performed for each particle size range using Cu K-α radiation (λ = 1.5418 Å) and an image plate detector over the 2θ range of 10–100° in the reflection mode. The XRD measurements were carried out both before and after the heat treatment. The XRD spectra were refined using the Rietveld method and analyzed using the diffraction software MAUD [26–28]. The anisotropic crystallite sizes were modeled using the Popa approach [29], which was implemented in MAUD. Popa developed a model that is compatible with the Rietveld method to describe the anisotropic broadening of the diffraction peaks caused by crystallite sizes and microstrain, which is generally invariant with respect to the Laue group.

3. Results

Fig. 1 depicts the crystallite size and microstrain as functions of the milling time. As expected, increasing the milling time decreased the crystallite size of the powders, whereas the microstrain increased.

The particle size distributions of the as-atomized and milled powders are illustrated in Fig. 2. As a result of the milling process, the 20-h-milled powder has a higher fraction of the finest particles (<25 μm) with a correspondingly lower amount of the biggest particles (>45 μm).

SEM images of the particles of the powder corresponding to different size ranges are shown in Fig. 3. Fig. 3(a) shows the as-atomized powder, while Fig. 3(b), (c), and (d) show the 20 h-milled powder samples with sizes of <25 μm, 25–45 μm, and 45–90 μm, respectively. The flake-like morphology of the particles of the milled powder indicates that even after 20 h of milling, the particles of the powder are yet to achieve round shapes [30].

Table 1 illustrates the crystallite size and microstrain of the particles for the three size ranges after milling for 20 h. While

the crystallite size increases with increasing particle size of the powder, the corresponding microstrain decreases from 0.26% for the smallest powder particles to 0.17% for the biggest granules.

The DSC curves of the as-atomized and milled powders (<25 μm, 25–45 μm, and 45–90 μm) are shown in Fig. 4. The curves are characterized by the presence of two peaks indicated by the numbers 1 and 2, relating to the transformations of GP zones and coherent precipitates, respectively.

In order to study the evolution of the microstructure with heat treatment, XRD analysis was carried out on the as-milled and heat-treated powders. XRD spectra of the as-milled powders are displayed in Fig. 5, while the XRD spectra of the finest milled powder heated at 475 °C for 5, 10, 15, and 20 min are depicted in Fig. 6. The spectra of the as-milled powders display only the Al peaks for all the milling times, while other peaks appear after the heat treatments, as observed in Fig. 6. The peaks corresponded to two different intermetallic phases (θ and S).

XRD spectra were used to determine the amount of S and θ phases, which are reported in Figs. 7–9 for the milled powders with particle sizes ranging from 45 to 90 μm, 25–45 μm, and <25 μm, respectively. At each treatment temperature, a decrease of S phase and an increase of θ phase is observed for the three granulometric fractions with time. The influence of the heat treatment temperature and the difference between the three granulometric fractions of the powders is discussed in the next section.

4. Discussion

It is evident from Fig. 1 that there was a sharp decrease in the crystallite size between 3 and 6 h of milling, whereas between 6 and 9 h of milling, the crystallite size decreased at a moderate rate. Beyond 9 h of milling, the rate of decrease was even lower. Therefore, a general trend of reduction of the crystallite size with the milling time was observed, displaying a reduction of approximately 68 nm between 3 and 20 h of milling; after 20 h of milling, the average size of the crystallites was 58 nm. However, the size curve did not reach a plateau.

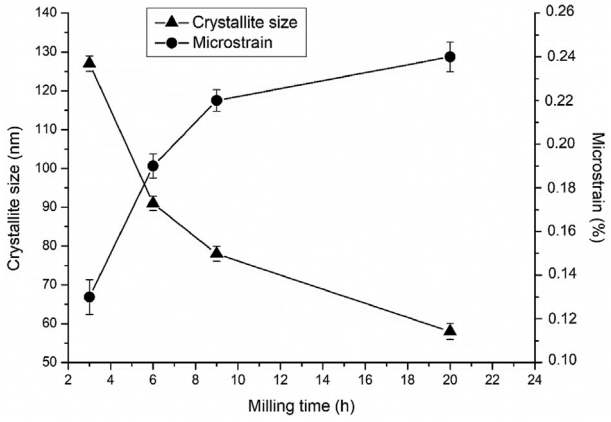

Fig. 1 – Crystallite size and microstrain of the as-milled alloy powders as functions of milling time.

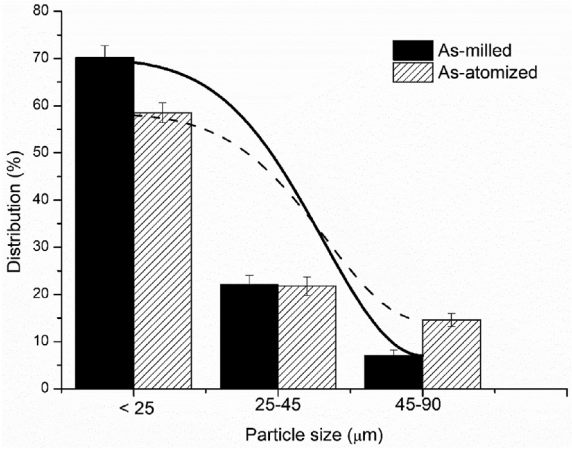

Fig. 2 – Particle size distributions (wt%) of as-atomized and 20-h-milled alloy powders. The normal curves were plotted using distribution points for each particle sizes.

Because of the mechanical deformation of the powder particles during milling, as the crystallite size decreased, the internal crystallite strain (microstrain) increased, reaching a value of 0.24% after 20 h of milling. This was in line with the results described by Jafari et al. [14].

Fig. 2 shows that the most of the particles were smaller than 25 μm for both the as-atomized and the milled powders. Further, as evident from the figure, the milling process resulted in an increase in the proportion of smaller particles (<25 μm) from 58 to 70%. At the same time, the proportion of the largest particles (45–90 μm) reduced from 15% to approximately 7%. The particle size distribution for both as-atomized and milled powders shows that the particles of size <25 μm were in higher quantities, and the percentage of particles smaller than 25 nm was higher in the milled powder as compared to that in the as-atomized powder. This is highlighted by the steeper curve for the milled powders observed in Fig. 2.

The differences in the particle size can be seen clearly in the images of Fig. 3. While the as-atomized particles (Fig. 3(a)) are spherical, they become flattened after the milling process (Fig. 3(b), (c), and (d)); this is true for all the size ranges. Moreover, the morphologies of the milled powder particles are similar. These data agree with those shown in the graph of Fig. 1, which indicates that even after 20 h of milling the crystallite size did not reach a plateau, indicating that the particles were still undergoing shape transition. Milling initially results in the plastic deformation of the particles and their subsequent flattening, which is followed by fragmentation into rounder particles as the milling progresses [30].

As expected, the crystallite size decreased and the microstrain increased with a decrease in the particle size, as shown in Fig. 1. The structural characteristics of the powder obtained after milling were different from those reported in the literature [31,32]. In particular, the average size of the crystallites was larger (51 vs 30 nm) and the microstrain was smaller (0.26 vs 0.4%). Additionally, the morphology of the milled powder particles, shown in Fig. 3, together with the particle size

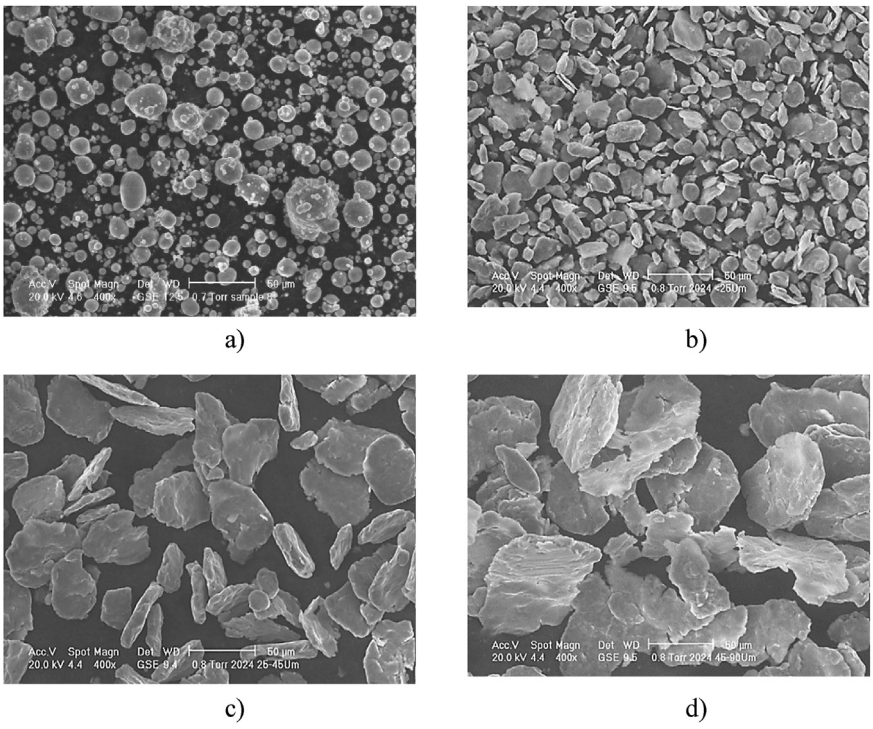

Fig. 3 – SEM micrographs of alloy particles corresponding to different size ranges: (a) as-atomized and (b) (c) (d) after milling for 20 h and corresponding to sizes of (b) < 25 μm, (c) 25–45 μm, and (d) 45–90 μm.

distribution, shown in Fig. 2, indicate that it is possible to decrease both the particle and crystallite sizes by extending the milling time. However, for the three particle size ranges considered in this study, the crystallite sizes were on the nanometer scale. These size ranges were suitable for studying the effects of the powder particle nanostructure on the phase transformations that occur during heat treatments.

As observed in Fig. 4, the DSC curve of the as-atomized powder contains two distinct peaks: an extended exothermic peak between 225 and 330 °C (peak 1) and another exothermic peak between 480 and 520 °C (peak 2). These are attributable to the transformations involving GP zones and coherent precipitates, respectively, as also reported by Badini et al. [15] and Murayama et al. [19]. The shift in the peaks to lower temperatures in the case of the milled powder samples (between 220 and 280 °C) can be attributed to the accumulated deformation energy, since the milled powder samples ought to exhibit a large lattice strain owing to the reduction in the grain size to the nanoscale during milling. A similar behavior was also observed by Badini et al. [15] in an Al–SiC composite in the deformed areas close to the interface between the reinforcement particles and the metallic matrix. However, for all three particles size ranges, the exothermic peaks occurred at the same temperature, thus confirming that the magnitude of the deformation introduced by the milling process did not have any effect.

In the case of peak 2, a comparison of the as-atomized powder curve with those of the milled ones shows that peak 2 is broader in the case of the milled powders because it starts at a slightly lower temperature. There is also a higher exothermic effect in the milled powder curves. Peak 2 is attributed to the precipitation of the incoherent θ/S phases, and its larger energetic contribution in the case of the milled powders suggests the precipitation of a higher amount of particles in it compared to that in the as-atomized powder.

The effect of the temperature and milling time on the precipitation amount was analyzed, while considering the influence of the powder nanostructure on the heat treatment transformations of the Al alloy (Figs. 7–9). Since it is difficult to detect coherent precipitates using the conventional XRD technique, the XRD analysis focused on the incoherent precipitates, as shown in Fig. 6, which demonstrates the progressive disappearance of the peaks of the S phase with increasing time at 475 °C. Considering that the heat treatment temperatures investigated are significantly higher than the typical aging temperature of the alloy and are rather similar to the solubilization temperature in a conventional precipitation hardening treatment, the transformations induced by the heat treatments must therefore be the result of the evolution of the low-temperature precipitates during heating, whose formation is enhanced by the nanostructure.

It can be seen from Figs. 7–9 that two incoherent precipitates (θ and S) were detected. The θ phase was Al_2Cu, with

Table 1 – Crystallite size and microstrain of alloy particles of different size ranges.

Particle size (μm)	Crystallite size (nm)	Microstrain (%)
<25	51 ± 1.82	0.26 ± 0.02
25–45	63 ± 2.70	0.21 ± 0.01
45–90	78 ± 2.12	0.17 ± 0.01

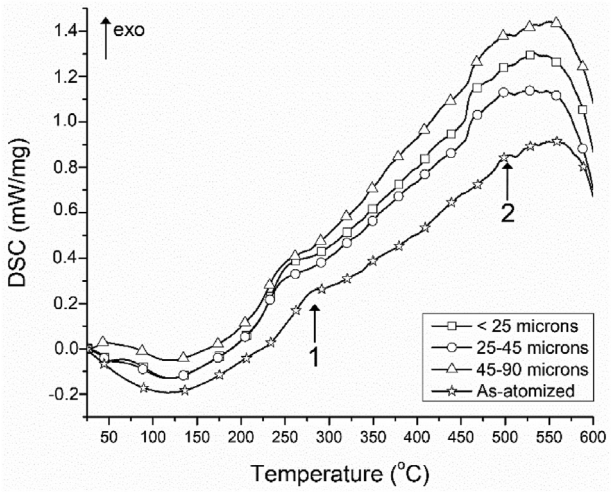

Fig. 4 – DSC curves of as-atomized and milled powders sizing range <25 μm, 25–45 μm, and 45–90 μm.

a body-centered tetragonal lattice structure, while the S phase had the stoichiometric composition Al_2CuMg and an orthorhombic lattice structure. In the as-milled powder, both S and θ phases were not detected by XRD, as shown in Fig. 5, confirming that the powder was a supersaturated solid solution.

Fig. 7 shows the results of the XRD analysis of the coarsest powder. The volume fraction of the S phase decreases and that of the θ phase increases over time. The effect of temperature is not monotonic, since phase fraction data measured at the highest temperature are intermediate between those measured at 475 (highest amount of S and lowest amount of θ) and 500 °C (lowest amount of S and highest amount of θ at the same time). The same trend is seen in Fig. 8 for the intermediate temperature, but the magnitude of increase in θ and decrease in S with time are more pronounced. The effect of temperature is monotonic, i.e., the increase in temperature increases θ and decreases S. In the finest powder (Fig. 9) the trends are even more pronounced; no S phase is present at 525 °C and at 500 °C for 10 min and at 475 °C for 20 min, while θ increases with time only at 475 °C. At the other two temperatures (500 and 525 °C), θ decreases with time at 525 °C and exhibits a maximum for 15 min at 500 °C. The influence of temperature is almost monotonic.

In general, the results suggest that heat treatments cause a progressive replacement of the S phase with the θ phase that is followed by a dissolution of the θ phase. These phenomena are promoted by temperature and time and are enhanced by the decrease of the particle size, that is, by a reduction in the crystallite size and/or an increase of the lattice strain. This internal accumulated energy accelerates the transformation from the S phase to the θ phase and the dissolution of the latter. The effect is particularly evident in the case of the finest powder, which neither contained the S phase at 525 °C nor after heating at 500 °C for 10 min and shows the decrease of the volume fraction of the θ phase at the same temperature.

Jafari et al. [14] performed a similar analysis on an Al–Cu–Mg alloy powder produced by mechanical milling and observed that the S phase was present up to 350 °C, while the θ phase was stable up to 550 °C. However, the XRD spectra of the alloy components were not quantitatively elaborated in their study. The thermodynamic equilibrium predicted in their study using the TCAL4 database showed a continuously decreasing fraction of the S phase from 100 up to 480 °C, while the fraction of the θ phase increased up to about 400 °C, and then decreased to a residual fraction at the melting point [32]. The results of the present investigation are in good agreement with those results. At the heat treatment temperatures that are closer to the solubilization temperature than the aging temperature, the microstructural evolution is a result of the precipitation occurring during heating that leads to the formation of the incoherent precipitates and their progressive dissolution in the matrix. Such a dissolution begins with the S phase, which is followed by the formation of an increasing amount of the θ phase and its subsequent dissolution. The transformation from S to θ was attributed by Jafari et al. [14] to the lower diffusivity of Mg compared to Cu in the Al matrix because of its greater atomic volume. However, Styles et al. [33] reported the activation energy of the bulk diffusivity of Cu and Mg in Al to be 136 and 131 kJ/mol, respectively. This small but significant difference makes the bulk diffusivity of Mg in Al greater than that of Cu, which was also confirmed by Du

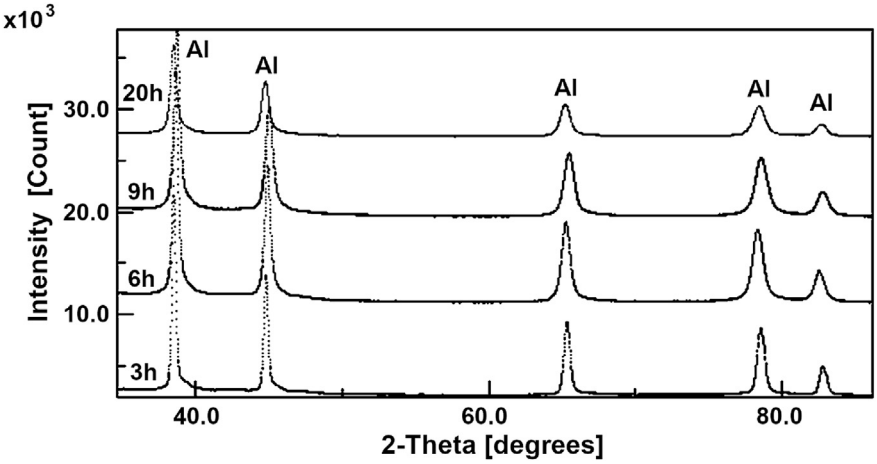

Fig. 5 – XRD spectra of the as-milled powders for different milling times.

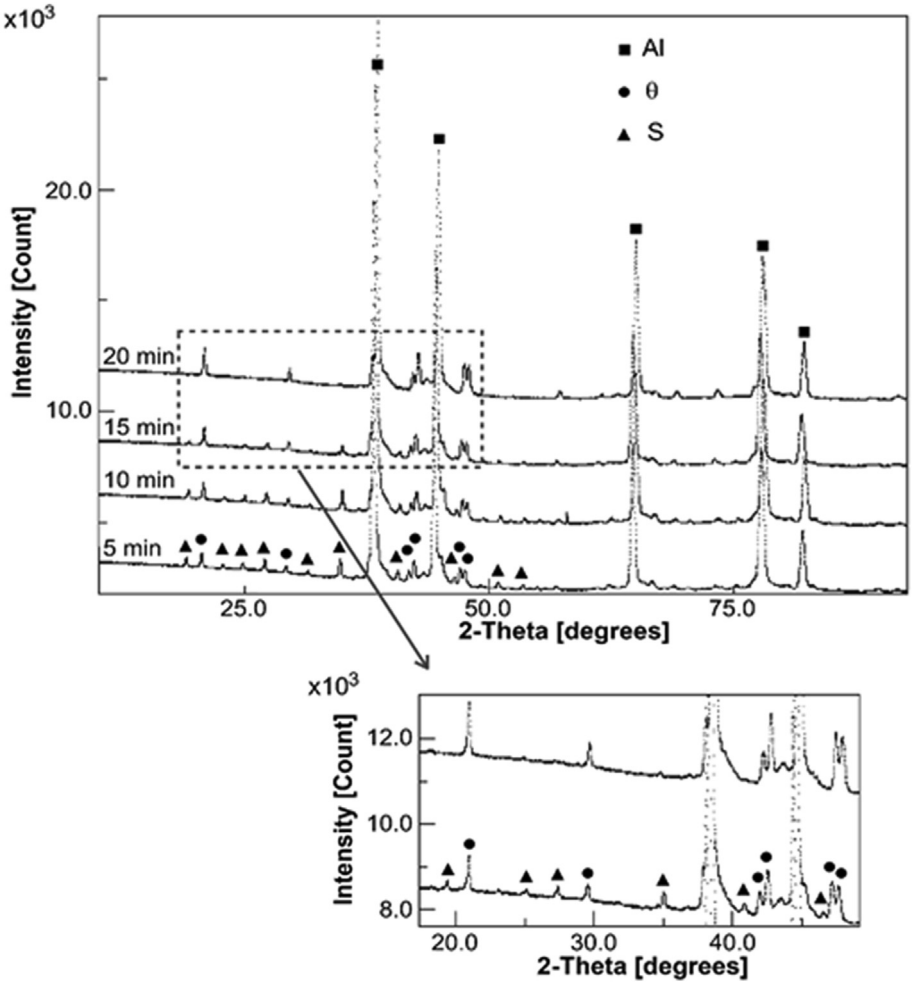

Fig. 6 – XRD spectra of powder of size smaller than 25 μm heat-treated at 475 °C for 5, 10, 15, and 20 min.

et al. [34] The higher diffusivity of Mg compared to Cu in the Al matrix may be responsible for the progressive replacement of S with θ during precipitate dissolution, because dissolution is favored by the diffusivity of the solute atoms in the matrix. The higher the diffusivity, the faster the dissolution, because elements of low diffusivity tend to segregate at the interface between the precipitate and the matrix, thus slowing down the progress of the dissolution [35]. The lattice strain of the milled powder promotes the transformations due to the pipe diffusion mechanism of the dislocation. It is well known that atomic migration in solids is much more rapid along or near the dislocations than through the regular lattice [36]. Dislocation density, ρ (m-2), can be calculated through [37]:

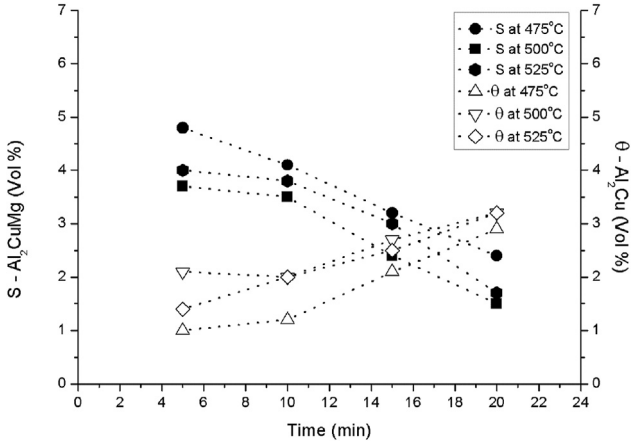

Fig. 7 – Volume fractions of S (Al_2CuMg) and θ (Al_2Cu) precipitates in the size range 45–90 μm as functions of heating time at 475, 500 and 525 °C, for 5, 10, 15 and 20 min.

$$\rho = \left[\left(2\sqrt{3}\right) / (Db)\right] * \left[\left(\varepsilon^2\right)^{1/2}\right] \quad (1)$$

where ε is the microstrain (%), D is the average grain size (m), and b is the magnitude of the Bürger's vector (0.286×10^{-9} m). The dislocation density values obtained for the different granulometric fractions of the powder were 6.2×10^{16}, 4.04×10^{16}, and 2.64×10^{16} m^{-2} for the particle size ranges of <25, 25–45, and 45–90 μm, respectively. The dislocations contribute significantly to the diffusion of the different atoms in the Al matrix. Also, the vacancies created by the plastic deformation can increase the diffusivity of the atoms that promotes the decomposition of the supersaturated solid solution at a low temperature, with a consequent precipitation

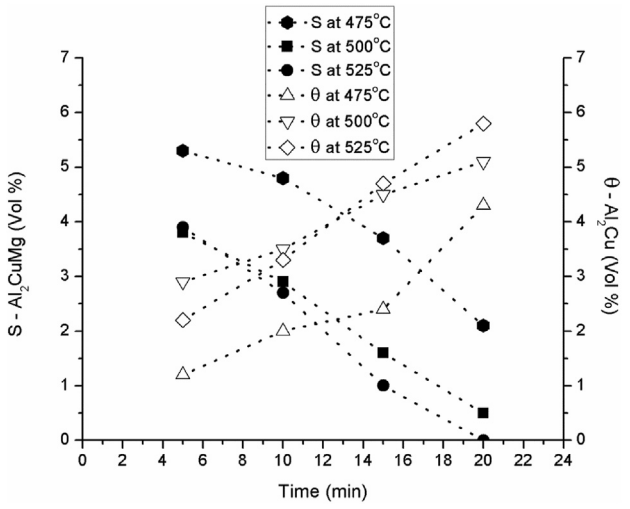

Fig. 8 – Volume fractions of S (Al_2CuMg) and θ (Al_2Cu) precipitates in the size range 25–45 μm as functions of heating time at 475, 500 and 525 °C, for 5, 10, 15 and 20 min.

of the intermetallic phases and their dissolution at higher temperatures. In the finest powder particles, the strain-induced vacancies and dislocations lead to an accelerated diffusion of atoms that results in a faster dissolution of the S phase.

5. Summary and conclusions

In this study, a nanostructured 2024 Al powder has been produced by mechanical milling and characterized by considering its microstructural evolution in its typical sintering temperature range. The study is summarized as follows:

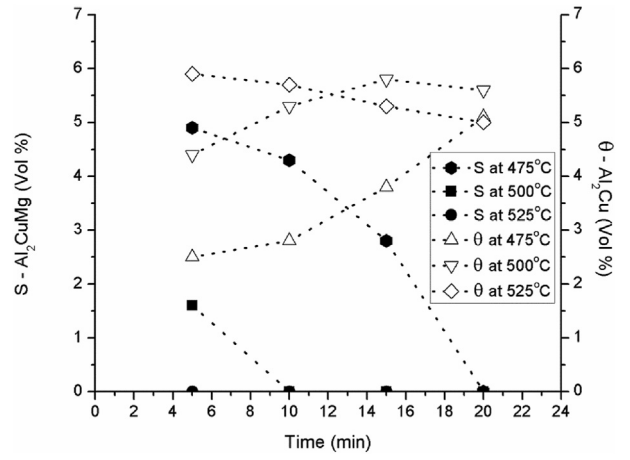

Fig. 9 – Volume fractions of S (Al_2CuMg) and θ (Al_2Cu) precipitates as functions of time for particles smaller than 25 μm in size as a function of heating time at 475, 500 and 525 °C, for 5, 10, 15 and 20 min.

- With decreasing powder particle size, the size of the crystallite also decreased. Furthermore, this reduction in the crystallite size was attributed to the increase in the number of defects in the lattice structure during the deformation and the fragmentation of the powder particles during the milling process.
- The morphology of the milled powder particles indicated that the particle refinement process had not completed, since the particles exhibited a flake-like morphology, whereas for longer times, it was expected to become round and finer.
- The results of the DSC analysis indicated the precipitation and dissolution of GP, coherent, and incoherent precipitates in the as-atomized and as-milled powders. Formation and dissolution of incoherent θ/S phases were observed in the case of the milled powders.
- The transition from the Al_2CuMg (S) phase to the Al_2Cu (θ) phase occurred earlier in the case of the finer powder particles due to the promotion of the transformation by the higher accumulated deformation energy that contributed to accelerate this process via dislocation pipe diffusion and vacancies.

Declaration of Competing Interest

The authors declare that they have no known competing financial interests or personal relationships that could have appeared to influence the work reported in this paper.

Acknowledgements

We wish to thank Dr. Gloria Ischia, Dr. Lorena Maines, Dr. Ivan Lonardelli and Dr. Nerio Vicente Junior for their contribution to this project. There is no funding to declare.

REFERENCES

[1] Krymskiy S, Sitdikov O, Avtokratova E, Markushev M. 2024 aluminum alloy ultrahigh-strength sheet due to two-level nanostructuring under cryorolling and heat treatment. Trans Nonferrous Metals Soc China 2020;30:14–26. https://doi.org/10.1016/S1003-6326(19)65176-9.

[2] Yin J, Lu J, Ma H, Zhang P. Nanostructural formation of fine grained aluminum alloy by severe plastic deformation at cryogenic temperature. J Mater Sci 2004;39:2851–4. https://doi.org/10.1023/B:JMSC.0000021463.83899.b3.

[3] Moreno-Valle EC, Sabirov I, Perez-Prado MT, Murashkin MY, Bobruk EV, Valiev RZ. Effect of the grain refinement via severe plastic deformation on strength properties and deformation behavior of an Al6061 alloy at room and cryogenic temperatures. Mater Lett 2011;65:2917–9. https://doi.org/10.1016/j.matlet.2011.06.057.

[4] Molinari A, Demetrio K, Lonardelli I, Menapace C, Zadra M. Spark plasma sintering of nanostructured aluminum powders produced by cryomilling. In: Advances in powder metallurgy and particulate materials - 2009, proceedings of the 2009

international conference on powder metallurgy and particulate materials. Las Vegas: EUA: Powder Met.; 2009. p. 72–8.
[5] Demétrio KB, Molinari A. Thermal stability and microstructure of nanometric 2024 aluminum alloy powder obtained by cryogenic milling and spark plasma sintering. Mater Res 2018;21(6):1–10. https://doi.org/10.1590/1980-5373-mr-2018-0182.
[6] Khor KA, Cheng KH, Yu LG, Boey F. Thermal conductivity and dielectric constant of spark plasma sintered aluminum nitride. Mater Sci Eng, A 2003;347:300–5. https://doi.org/10.1016/S0921-5093(02)00601-9.
[7] Anselmi-Tamburini U, Garay J, Munir ZA, Tacca A, Maglia F, Chiodelli G, et al. Spark plasma sintering and characterization of bulk nanostructured fully stabilized zirconia: Part II. Characterization studies. J Mater Res 2004;19:3263–9. https://doi.org/10.1557/JMR.2004.0424.
[8] Fujii T, Tohgo K, Isono H, Shimamura Y. Fabrication of a PSZ-Ti functionally graded material by spark plasma sintering and its fracture toughness. Mater Sci Eng, A 2016;682:656–63. https://doi.org/10.1016/j.msea.2016.11.091.
[9] Fujii T, Tohgo K, Putra PB, Shimamura Y. Fabrication of alumina-PSZ composites via spark plasma sintering and their mechanical properties. J Mech Behav Biomed Mater 2019;91:45–53. https://doi.org/10.1016/j.jmbbm.2018.11.028.
[10] Brochu M, Zimmerly T, Ajdelsztajn L, Lavernia EJ, Kim GE. Dynamic consolidation of nanostructured Al-7.5%Mg alloy powders. Mater Sci Eng 2007;466:84–9. https://doi.org/10.1016/j.msea.2007.02.028.
[11] Sasaki TT, Hono K, Vierke J, Wollgarten M, Banhart J. Bulk nanocrystalline Al85Ni10La5 alloy fabricated by spark plasma sintering of atomized amorphous powders. Mater Sci Eng 2009;490:343–50. https://doi.org/10.1016/j.msea.2008.01.059.
[12] Vintila RR, Drew RAL, Brochu M. Nanostructured NS Al-2024 alloy fabricated by cryogenic milling and consolidated via spark plasma sintering. In: Advances in powder metallurgy and particulate materials: proceedings of the 2010 international conference on powder metallurgy & particulate material. Princeton, USA: Metal Powder Industries Federation; 2010. p. 948–60.
[13] Moelle CH, Fecht HJ. Thermal stability of nanocrystalline iron prepared by mechanical attrition. Nanostruct Mater 1995;6:421–4. https://doi.org/10.1016/0965-9773(95)00086-0.
[14] Jafari M, Enayati MH, Abassi MH, Karimzadeh F. Thermal stability and structural changes during heat treatment of nanostructured Al2024 alloy. J Alloys Compd 2009;478:260–4. https://doi.org/10.1016/j.jallcom.2008.12.017.
[15] Badini CF, Marino F, Verné E. Calorimetric study on precipitation path in 2024 alloy and its SiC composite. Mater Sci Eng 1995;191:185–91. https://doi.org/10.1016/0921-5093(94)09637-C.
[16] Kumar PRS, Kumaran S, Srinivasa RT, Sivaprasad K. Microstructure and mechanical properties of fly ash particle reinforced AA6061 composites produced by press and extrusion. Trans Indian Inst Met 2009;62:559–66. https://doi.org/10.1007/s12666-009-0094-x.
[17] Totten GE, Mackenzie DS. Handbook of aluminum. New York: Marcel Dekker; 2003.
[18] Koch CC. The synthesis and structure of nanocrystalline materials produced by mechanical attrition: a review. Nanostruct Mater 1993;2:109–29. https://doi.org/10.1016/0965-9773(93)90016-5.
[19] Murayama M, Horita Z, Hono K. Microstructure of two-phase Al-1.7 at% Cu alloy deformed by equal-channel angular pressing. Acta Mater 2001;49:21–9. https://doi.org/10.1016/S1359-6454(00)00308-6.
[20] Jena AK, Gupta AK, Chaturvedi MC. A differential scanning calorimetric investigation of precipitation kinetics in the Al-1.53 wt% Cu-0.79 wt% Mg alloy. Acta Metall 1989;37:885–95. https://doi.org/10.1016/0001-6160(89)90015-1.
[21] Lee Z, Witkin DB, Radmilovic V, Lavernia EJ, Nutt SR. Bimodal microstructure and deformation of cryomilled bulk nanocrystalline Al-7.5Mg alloy. Mater Sci Eng 2005;410–411:462–7. https://doi.org/10.1016/j.msea.2005.08.104.
[22] Zhou F, Witkin DB, Nutt S, Lavernia EJ. Formation of nanostructure in Al produced by a low-energy ball milling at cryogenic temperature. Mater Sci Eng 2004;375–377:917–21. https://doi.org/10.1016/j.msea.2003.10.235.
[23] Witkin DB, Lavernia EJ. Synthesis and mechanical behavior of nanostructured materials via cryomilling. Prog Mater Sci 2006;51:1–60. https://doi.org/10.1016/j.pmatsci.2005.04.004.
[24] Papazian JM. Effects of SiC whiskers and particles on precipitation in aluminum matrix composites. Metallurgical transactions A 1988;16:2945–53. https://doi.org/10.1007/BF02647721.
[25] Khitouni M, Daly R, Kolsi AW, Njah N. X-ray studies of structure defects in nanostructured Al-4wt%Cu alloy. Phys Status Solidi 2006;3:3341–6. https://doi.org/10.1002/pssc.200567053.
[26] Lutterotti L, Matthies S, Wenk HR, Schultz AS, Richardson JJW. Combined texture and structure analysis of deformed limestone from time-of-flight neutron diffraction spectra. J Appl Phys 1997;81:594–600. https://doi.org/10.1063/1.364220.
[27] Lonardelli I, Wenk HR, Luterotti L, Goodwin MB. Texture analysis from synchrotron diffraction images with the Rietveld method: dinosaur tendon and salmon scale. J Synchrotron Radiat 2005;12:354–60. https://doi.org/10.1107/S090904950500138X.
[28] Molinari A, Lonardelli I, Demetrio K, Menapace C. Effect of the particle size on the thermal stability of nanostructured aluminum powder: dislocation density and second-phase particles controlling the grain growth. J Mater Sci 2010;45:6739–46. https://doi.org/10.1007/s10853-010-4768-x.
[29] Popa NC. The (hkl) dependence of diffraction-line broadening caused by strain and size for all laue groups in rietveld refinement. J Appl Crystallogr 1998;31:176–80. https://doi.org/10.1107/S0021889897009795.
[30] Suryanarayana C. Mechanical alloying and milling. Prog Mater Sci 2001;46:1–184. https://doi.org/10.1016/S0079-6425(99)00010-9.
[31] Hayes R, Tellkamp V, Lavernia E. A preliminary creep study of a bulk nanocrystalline Al-Mg alloy. Scripta Mater 1999;41:743–8. https://doi.org/10.1016/S1359-6462(99)00210-9.
[32] Zhang F, Levine LE, Allen AJ, Campbell CE, Creuziger AA, Kazantseva N, et al. In situ structural characterization of ageing kinetics in aluminum alloy 2024 across angstrom-to-micrometer length scales. Acta Mater 2016;111:385–98. https://doi.org/10.1016/j.actamat.2016.03.058.
[33] Styles MJ, Marceau RKW, Bastow TJ, Brand HEA, Gibson MA, Hutchinson CR. The competition between metastable and equilibrium S (Al2CuMg) phase during the decomposition of Al-Cu-Mg alloys. Acta Mater 2015;98:64–80. https://doi.org/10.1016/j.actamat.2015.07.011.
[34] Du Y, Zhang WB, Liu DD, Cui SL, Zhao DD, Zhang LJ, et al. Atomic mobility and diffusivity in Al alloys, NIST 2010 diffusion workshop. March 23-24, 2010 [Maryland, USA].
[35] Reed-Hill RE. Physical metallurgy principles. Boston, Massachusetts: PWS-KENT Publishing Company; 1973. p. 515–7.
[36] Nasedkina Y, Sauvage X, Bobruk EV, Murashkin M Yu, Valiev RZ, Enikeev NA. Mechanisms of precipitation induced by large strains in the Al-Cu System. J Alloys Compd

2017;710:736–47. https://doi.org/10.1016/j.jallcom.2017.03.312.
[37] Zhao YH, Lu K, Zhang K. Microstructure evolution and thermal properties in nanocrystalline Cu during mechanical attrition. Phys Rev B 2002;66(8):085404. https://doi.org/10.1103/PhysRevB.66.085404.